Multifunctional optical materials based on transparent inorganic glasses embedded with PbS QDs

Zheng Wang, Jiabo Li, Feifei Huang, Youjie Hua, Ying Tian, Xianghua Zhang, Shiqing Xu

Multifunctional Optical Materials Based on Transparent Inorganic Glasses Embedded with PbS QDs

Zheng Wang[a,b], Jiabo Li[a], Feifei Huang[a*], Youjie Hua[a], Ying Tian[a], Xianghua Zhang[b], Shiqing Xu[a*]

[a] *Key laboratory of Rare Earth Optoelectronic Materials and Devices of Zhejiang Province, Institute of Optoelectronic Materials and Devices, China Jiliang University, Hangzhou, 310018, China*

[b] *Laboratory of Glasses and Ceramics, Institut des Sciences Chimiques de Rennes , UMR CNRS 6226, University of Rennes 1, Rennes 35042, France*

Email: huangfeifei@cjlu.edu.cn & shiqingxu@cjlu.edu.cn

Abstract:

Quantum dot (QD)-embedded glass, which is a high-performance multifunctional optical material, has the combined advantages of excellent optical properties of QDs and easy processing of glass. In this study, an inorganic PbS QD embedded multicomponent glass, which produces variable emission at different ultraviolet (UV) excitation wavelengths, is synthesized. The samples are fabricated via a facile melt-quenching method and their structural, optical, photoluminescent, and morphological properties are discussed. The QD glass exhibits broad-band UV excitation in the range of 250–400 nm, and the full width at half maximum of the emission peaks of the QD glasses reaches 177.8 and 158.5 nm at room temperature under an excitation of 365 and 310 nm, respectively. Notably, white light emission with a high color rendering index is obtained under UV excitation at 350 and 365 nm

by doping blue light emitting rare earth (RE) Tm^{3+} ions into the system. The doped samples exhibit excellent color stability and their CIE coordinates shift along the Planck blackbody locus with increasing temperature. Further, based on the differences in the luminescence mechanisms of the PbS QDs and Tm^{3+} ions, the application potential of the RE-doped PbS QD-embedded glasses in optical thermometry is discussed. The results demonstrate the application potential of these optically multifunctional inorganic QD glasses in the fields of optical conversion, anti-counterfeiting, white light illumination, and non-contact optical temperature measurement.

Keywords: PbS QDs glass, Variable emission, High CRI white light, Optical thermometry

Introduction

Semiconductor quantum dots (QDs) have attracted considerable attention for several decades because of their quantum confinement-induced unique tunable optoelectronic properties[1], which have been successively employed in applications, such as optical color converters[2-4], solar cells[5-7], multicolor displays[8-9], and light-emitting diodes (LEDs)[10-12]. Continuous experimental and theoretical research efforts have been dedicated toward the synthesis and performance enhancement of the semiconductor QD materials[10, 13-15]. Various semiconductor QDs, such as carbon dots[16], IIB-VIA, IVB-VIA, I-III-VI groups[17], and halide perovskite QDs[18], with excellent optoelectronic properties have been successfully synthesized. However, colloidal QDs typically synthesized by wet chemical methods are sensitive to the

environment, and the commonly used encapsulation host materials, such as molecular polymers and sol-gel films, are chemically and mechanically unstable, which significantly restricts their application in multifunctional optoelectronic devices[19]. QDs glasses, a special type of glass-ceramic wherein the glass network former does not participate in crystallization, exhibit improved thermal and chemical stability, and are synthesized by the conventional co-melting method[20-22]. Thus, they have attracted considerable interest.

Luminescence properties of the QDs embedded in an inorganic glass, including the spectral range and luminescence intensity, are similar to those of the corresponding colloidal QDs[23]. Inorganic glasses can be synthesized easily and possess good optical properties, and their high density and uniform composition can protect the QDs from the surrounding environment[20]. Additionally, the size and distribution of the embedded QDs can be effectively controlled via appropriate heat treatment (HT), and the aggregation or dissolution of QD particles in a glass matrix can be effectively prevented[21]. Although heavy metal elements, such as Cd and Pb, are harmful to the human body and are not environmentally friendly, Cd or Pb-containing QD glass exhibits superior optical performance compared with other elements of the group[19]. Therefore, cadmium chalcogenide[24-27], lead chalcogenide[28-30], and lead halide perovskite QDs[8, 31-33] intercalated glasses are regarded as promising multifunctional optical materials. Xiang et al.[34-37] discussed the application of lead halide perovskite QDs glasses in solid-state lighting, multicolor displays, and color conversion. Research on lead chalcogenide QD glasses has focused primarily on their

application in fiber amplifiers and saturable absorbers in the field of infrared lasers, whereas less attention has been paid to multifunctional applications in the visible range[29, 38-41]. The bandgap of PbS can vary from 0.41 eV for bulk to approximately 3.7 eV for QDs of size 1 nm at room temperature[42-43]. A wide range of emission from the visible to the infrared region can be theoretically obtained through an appropriate synthetic route, which is beneficial for the development of multifunctional optical materials.

Commercial protocols demonstrate that ideal white light can be achieved by combining the broad-band yellow emission with the intense blue emission obtained at the same excitation wavelengths[44]. The inorganic amorphous glass embedded with PbS QDs is also a potential yellow luminescent center for white LEDs. Rare earth (RE) elements exhibit remarkable optical characteristics owing to their abundant energy level structures[45-46] and RE co-doped QD glasses can be used to tune the optical properties, which is beneficial for obtaining multifunctional optical materials. Luminescence-based thermometers have attracted attention for their non-contact temperature sensing, accuracy, and applicability at the micro- and nano-scale[47]. Because the RE ions and QD glasses have different luminescence mechanisms, whether the QD glasses doped with RE ions can be used as optical thermometers is worth exploring. In this study, an inorganic PbS QD multicomponent glass with broad-band emission was fabricated using a simple co-melting method. Subsequently, its structure and optical properties were characterized and are discussed herein. Combining the blue emission from the co-doped Tm^{3+} ions with the broad-band

yellow emission of the PbS QDs, white light with a high color rendering index (CRI) can be obtained under ultraviolet (UV) excitation. Finally, the thermal quenching properties of the Tm^{3+} ion-doped PbS QD glasses were investigated, and their potential applications in optical thermometers are discussed based on the temperature-dependent photoluminescence (PL) spectra.

Experimental

The nominal composition of the host glass used in this study was $20SiO_2$-$30GeO_2$-$10B_2O_3$-$15Al_2O_3$-$10ZnF_2$-10NaF-$5Na_2O$ ($1PbO/2ZnS/0.5Tm_2O_3$, in mol%). The nomenclature of the different doped samples is listed in Table S1. All the raw materials were uniformly mixed in an agate mortar, placed in a corundum crucible, and melted in a high resistance furnace at 1400 °C for 40 min. The obtained melt was quenched, pressed on a plate preheated to 400 °C, and subsequently annealed in an annealing furnace to obtain the initial samples (details of the processing conditions and the corresponding nomenclature are provided in the Supporting Information). For testing the phase structure and optical properties of the initial samples, they were subjected to appropriate cutting, grinding, or polishing processes.

Optical absorption spectra were recorded on a Hitachi U-4100 ultraviolet–visible–near-infrared (UV−VIS−NIR) spectrophotometer. The structural analysis of the samples was performed using X-ray diffraction (XRD) spectra obtained using a D/MAX2550pc diffractometer (Rigaku International Corp., Japan) with Cu $K_{\alpha 1}$ as the incident radiation source. To study the microstructure of the samples, scanning transmission electron microscopy (STEM) was used and images were obtained using

a Tecnai G2 F20 (FEI, USA) high-resolution transmission electron microscope (HR-TEM) operating at 200 kV with a current of approximately 50 pA. PL emission and excitation spectra were obtained using an FLSP1000 spectrometer (Edinburgh Instrument Ltd., UK) equipped with an Xe lamp as the excitation source. The decay lifetimes were obtained using a PL3-211-P spectrometer (HORIBA JOBIN YVON, USA) with a nano-LED (370 nm). The temperature-dependent and variable excitation wavelength luminescence properties were acquired using an EX 1000 spectrometer (Everfine, China).

Results and discussion

To investigate the optical properties of each sample, the UV–VIS–NIR absorption spectra of the different samples before and after HT were obtained, and the corresponding absorption bands were appropriately labeled. Figure 1a shows the absorption spectra of the glass samples without the Tm^{3+} ions. Evidently, none of the samples exhibited any distinct absorption peaks, except for the different UV cut-off absorptions. With the sequential addition of PbO and ZnS to the glass matrix, the UV cut-off absorptions of the corresponding glass samples exhibited a gradual increase. When Pb^{2+} ions were introduced (PbG/PbGH) into the glass matrix, owing to their larger ionic radii, their effect on the polarization of the electron shell of oxygen ions was small, which resulted in a lose electron shell structure of non-bridging oxygen ions. This resulted in an increase in the UV cut-off absorption wavelength of the samples. The electrophilic potential of S^{2-} ions was lower than that of the other anions; when Pb^{2+} ions and ZnS were introduced (PZ/PZH) into the glass matrix, the

UV cut-off absorption wavelength was further increased because of these superimposing effects. In addition, Rayleigh scattering due to the precipitation of PbS in QDs can lead to an increase in the UV cut-off absorption wavelength[48]. However, the UV cut-off absorption wavelength of the PZH sample did not change after the HT. Generally, the HT process can lead to the growth of a crystallite phase in an amorphous environment, which further leads to an increase in the UV absorption cut-off edge. A possible reason could be that at least PbS precipitated in the system during annealing of the samples, and the self-limiting effect of the glass system did not cause PbS to grow during the HT process[49].

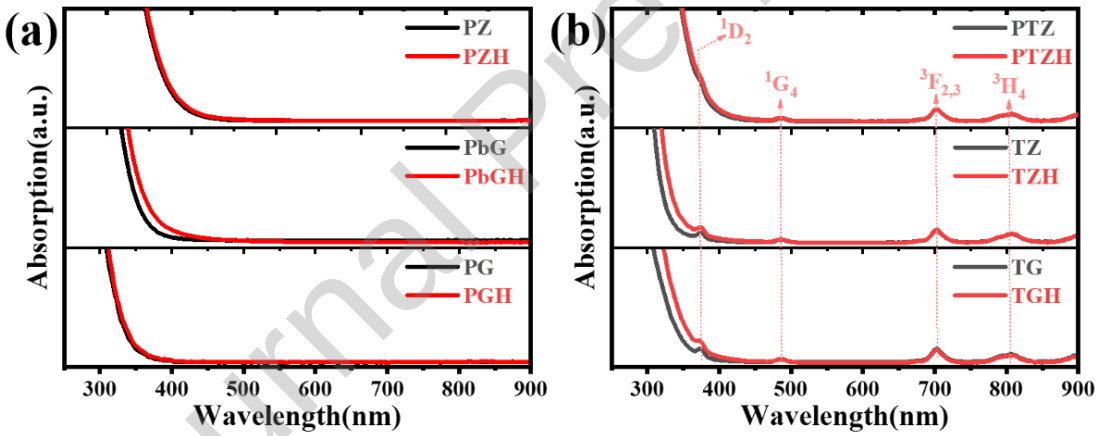

Figure 1. Absorption spectra of samples without Tm^{3+} ions (a) and doped with Tm^{3+} ions (b) under different conditions.

The absorption spectra of the samples doped with Tm^{3+} ions are shown in Figure 1b. All the samples exhibited four absorption bands centered at approximately 790, 686, 469, and 358 nm, representing transitions from the $^3H_6$ ground state of Tm^{3+} to the excited states $^3H_4$, $^3F_{2,3}$, $^1G_4$, and $^1D_2$[50], respectively. Notably, S^{2-} ions are less electrophilic than O^{2-} ions; therefore, the addition of ZnS resulted in a slight increase in the UV cut-off absorption wavelength. For the heat-treated TGH and TZH samples,

the main absorption band profiles did not change significantly relative to those of the TG and TZ samples, except for the increased UV cut-off absorption wavelength due to the HT. The absorption spectra of the PTZ and PTZH samples further revealed that the addition of Tm^{3+} ions had no additional effect on the samples, which was reflected in the typical absorption peaks of Tm^{3+} ions superimposed on the characteristic absorption spectra of PZ and PZH. All the samples exhibited excellent transparency in the visible range, which was additionally confirmed by the digital photographs shown in Figure S1.

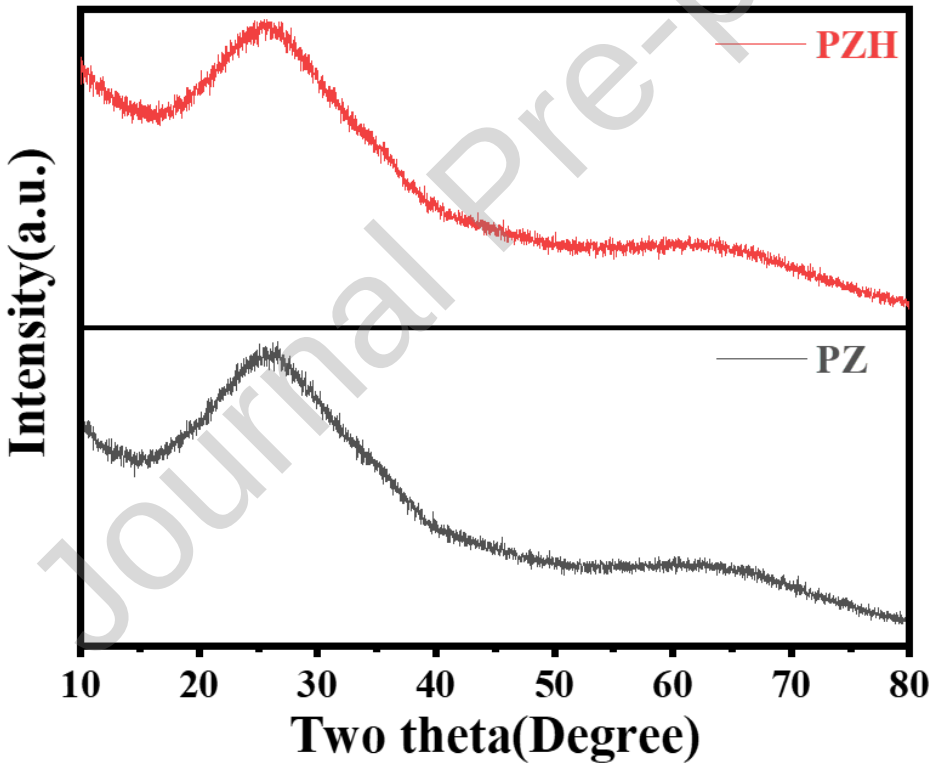

Figure 2 XRD patterns of the PZ and PZH samples.

XRD curves of the PZ and PZH samples were used to investigate the structure of the samples and verify the presence of PbS QDs in the glasses. However, both the XRD curves did not contain any distinct diffraction peak, as shown in Figure 2. The

broad humps were due to the amorphous structure of the synthetic matrix[51]. This was presumably caused by the small crystallite size and good dispersion of PbS, which needs to be subsequently confirmed by TEM analysis. The HR-TEM image of the PZ sample revealed numerous nano-crystalline phases uniformly distributed in the amorphous glass with a size less than 5 nm, as shown in Figure 3a. Moreover, the HR-TEM image showed clear crystal lattice fringes, and the spacing between the two crystal planes was approximately 0.342 nm, as shown in Figure 3b, which corresponded to the (1 1 1) crystal plane of PbS. The HR-TEM image of the PZH sample additionally revealed a similar crystal size and uniform distribution, but its crystal phase, lattice fringes, and diffraction patterns were comparatively clearer, as shown in Figures 3d–3f, respectively. The PZ and PZH samples were a composite of the polycrystalline and glass phases, as confirmed by the selected area electron diffraction (SAED) pattern shown in Figures 3c and 3f. Thus, the PbS crystal phase was separated from the glass system either during the hot-press molding or annealing process. The above results indicated that the PbS QDs were formed in the glass matrix in the annealing stage. Moreover, the high-temperature HT process only increased the amount and crystallinity of the PbS QDs but did not considerably increase their size because of the self-limiting effect brought about by the viscosity of the glass matrix[52]. Therefore, although the size of the QDs was very small and amorphous diffraction of the glass matrix produced a significant effect, the XRD of the sample after HT at a higher temperature(550 °C) could show weak characteristic diffraction peaks, corresponding to the JCPDS card number 78-1057[53], as shown in Figure S3.

Similarly, after HT at 550 °C, the crystal size of the PbS QDs did not increase significantly because of the self-limiting effect[49], as shown in Figure S4.

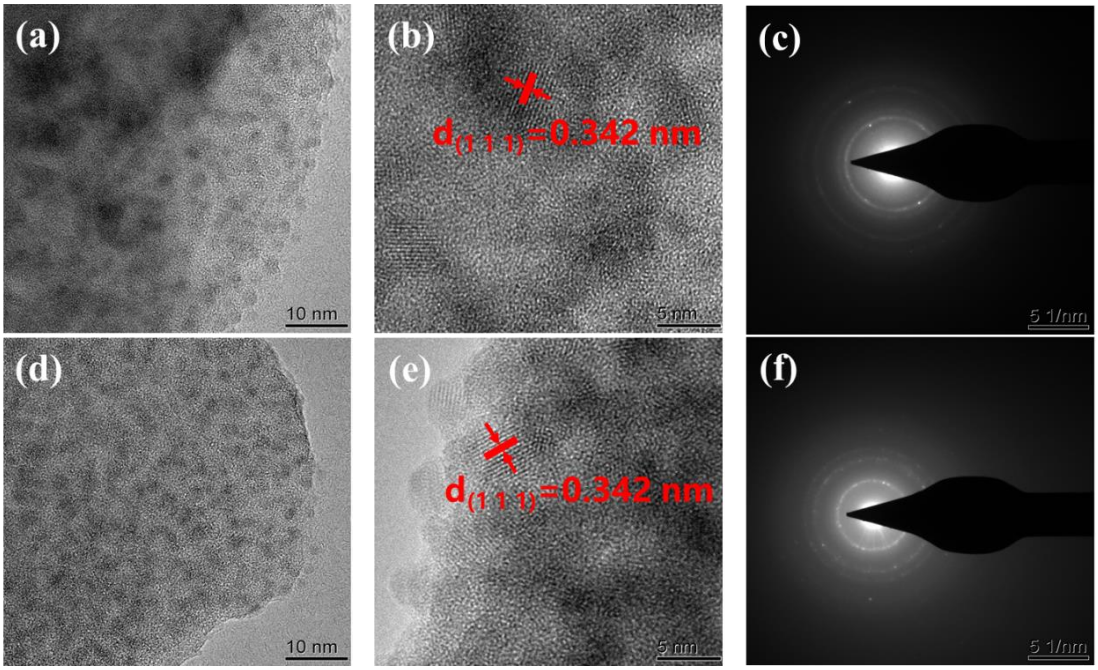

Figure 3 HR-TEM images and the corresponding SAED patterns of the (a)–(c) PZ and (d)–(f) PZH samples.

The digital photographs of the samples irradiated at 365 nm revealed that no distinct fluorescence emission was present in the PbO single-doped PbG or heat-treated PbGH samples, as shown in Figure S2. The ZG sample singly doped with ZnS exhibited a very weak purple emission, whereas the ZGH samples after HT exhibited a stronger red emission, which could be attributed to the recombination of electrons and vacancies in the valence band at the energy level of the defect state between the conduction band and valence band (usually related to S and Zn vacancies) of trace amounts of ZnS QDs or clusters present in the system[54-56]. The PbO and ZnS co-doped PZ and heat-treated PZH samples both exhibited yellowish-white fluorescence emission when irradiated by UV light, which could be attributed to the emission of

the PbS QDs formed in the glass host by the combination of PbO and ZnS. Notably, during the high-temperature melting process of this glass system, both PbO and ZnS are converted into their ionic forms, a mixture of O^{2-} and S^{2-} sites are the nearest neighbors of Pb^{2+}, and Pb^{2+} tends to bond with S^{2-} to form PbS[57]. The yellow emission could be caused by the quantum confinement effect or defects associated with the PbS QDs.

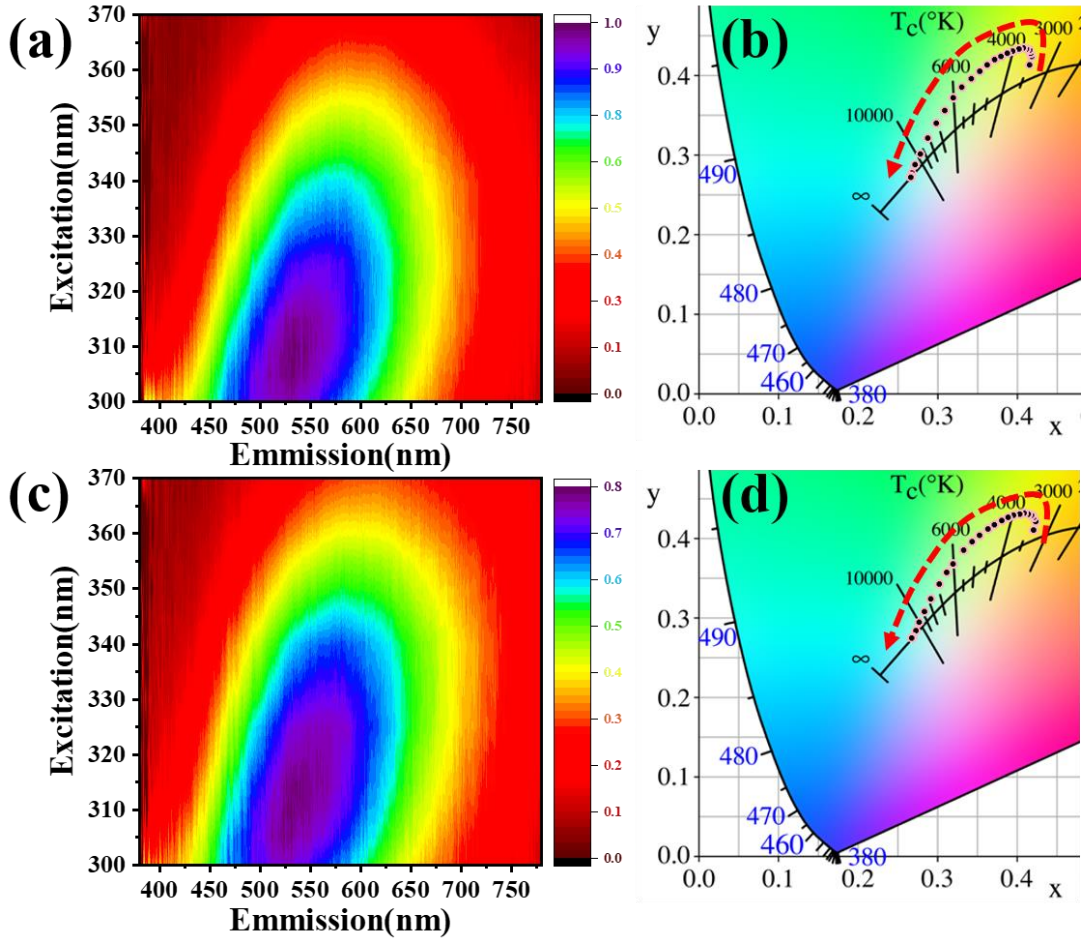

Figure 4. PL spectra of the (a) PZ and (c) PZH samples excited at wavelengths in the range of 300–370 nm. CIE coordinate diagrams of the (b) PZ and (d) PZH samples excited at wavelengths in the range of 260–370 nm, respectively.

Excitation wavelength-dependent PL spectra were used to explore and explain the origin of the yellow luminescence of the PZ and PZH samples, as shown in

Figures 4a and 4c, respectively. Both the samples exhibited broad-band luminescence covering nearly the entire visible range, which was inconsistent with the intrinsic exciton emission of the QDs[58]. Additionally, the excitation-dependent PL emission spectra exhibited a blue shift as the excitation wavelength decreased, which was associated with the phenomenon of self-trapped emission in defects[59]. The dotted-line graph of the emission peak as a function of the excitation wavelength shown in Figure S5a distinctly demonstrates the dependence of the emission peaks on the excitation wavelength. The properties of the PbS QDs in multicomponent glasses are bound to be influenced by a variety of system elements, including various dangling bonds on the crystal surface and substitution of elements with the similar valence state and ionic radii in the crystal phase, thus resulting in abundant surface or internal defects. These defects receive amorphous environmental protection and result in stable physicochemical properties. Therefore, after being excited by UV light, these defects can trap excitons, thereby exhibiting stable broadband emission. For the present system, the surface and interior of the PbS QDs had numerous defects; therefore, the emission spectra were dominated by the emission from the defect trapping states. The luminescence intensity of the PZH sample was slightly weaker than that of the PZ sample because the HT enhanced the crystallinity of the PbS QDs and reduction of the defect states, as shown in Figure S5b, which reveals the dependence of the emission peak intensity on the excitation wavelength. As shown in Figures 4b and 4d, with a decrease in the excitation wavelength, the corresponding CIE coordinate diagrams of the two samples gradually shifted from the yellow to blue-light region, which

indicated these samples have great potential for utilization in anti-counterfeiting applications as tunable luminescent materials.

The excitation spectra in the range of 225–425 nm for the PZ and PZH samples monitored at a wavelength of 560 nm are shown in Figure S6a. Both the PZ and PZH samples exhibited a broad excitation band with the center at approximately 310 nm. The broadband excitation and emission spectra revealed that the luminescence phenomenon in the present samples is very different from that of ions or band-edge luminescence. Figures 5a and 5b present the comparison of the PL spectra of the PZ and PZH samples at low (20 K) and room temperatures (300 K) after excitation at 310 and 365 nm, respectively. At low temperature the PL peaks exhibited an obvious red-shift and enhanced luminescence intensity compared with those at the room temperature. Generally, the bandgaps of most bulk semiconductors and QDs increases with temperature owing to thermal expansion, which result in a temperature-dependent change in the position of the luminescence peaks[39]. Moreover, owing to the high phonon energy and strong electron-phonon coupling in an oxidized glass, non-radiative relaxation easily occurs, which reduces the PL quantum efficiency. The intensity of the temperature-dependent PL spectra is determined by the defect trap state, and the PL intensity of QDs without surface defects is independent of the temperature. At low temperatures, thermal escape is suppressed, excitons are easily captured by the trap states of the QDs in the glass, and the electrons captured by the trap states are released to the ground state, thereby resulting in PL. As the temperature increases, thermal escape occurs, and the excitons trapped in the trap states are

consumed by thermal escape; thus, the PL intensity decreases with increasing temperature. Furthermore, owing to the complex and abundant energy level distribution of the defect states of the PbS QDs in the multi-component glass, the PbS QDs glasses exhibited broad-band emission at both room and low temperatures, and the maximum full width at half maximum (FWHM) was 158.5 and 177.8 nm corresponding to 310 and 365 nm pumping at 300 K, respectively. The broad-band excitation, emission spectra, and large Stokes shift characteristics of the PbS QDs in the glass are also beneficial for applications in optical color conversion devices[3-4].

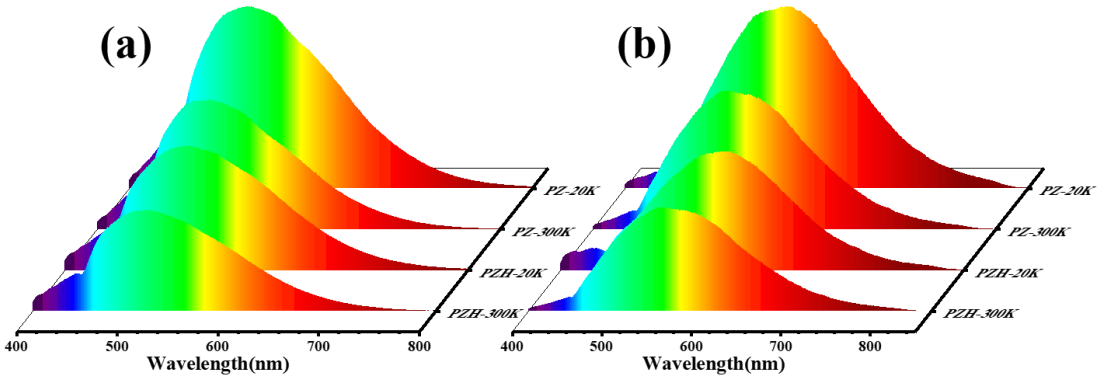

Figure 5. PL spectra of the PZ and PZH samples at an excitation wavelength of (a) 310 and (b) 365 nm at different temperatures.

To easily and effectively obtain white light emission with a high CRI, Tm^{3+} ions were introduced into the system as dopants because they are less affected by the host environment and can produce distinct blue light emission under UV excitation. The PL spectra of every luminescent sample were recorded at an excitation wavelength of 365 nm, as shown in Figure S7. All the Tm^{3+}-doped samples exhibited narrow-band blue light emission with a peak at 458 nm and a weak peak at 478 nm, which could be attributed to the energy level transitions of Tm^{3+}: $^1G_4 \rightarrow {}^3H_6$ and $^1D_2 \rightarrow {}^3F_4$[60],

respectively. In addition to the characteristic emission of the Tm^{3+} ions, the TZ and HT-TZH samples also exhibited a weak ZnS luminescence peak at approximately 420 nm, which is the reason behind the blue-violet emission of the actual samples under UV light irradiation. After the introduction of Tm^{3+} ions, the emission spectra of the PTZ and heat-treated PTZH samples consisted of the characteristic emission of the Tm^{3+} ions and PbS QDs, thereby resulting in bright white light emission. However, the characteristic emission of the PbS QDs was significantly weaker than that of the PZ and PZH samples, which could be due to some energy cross-transfer between the Tm^{3+} ions and PbS QDs, which is not conducive to the radiative transition (RT) between them. However, this requires further research and verification.

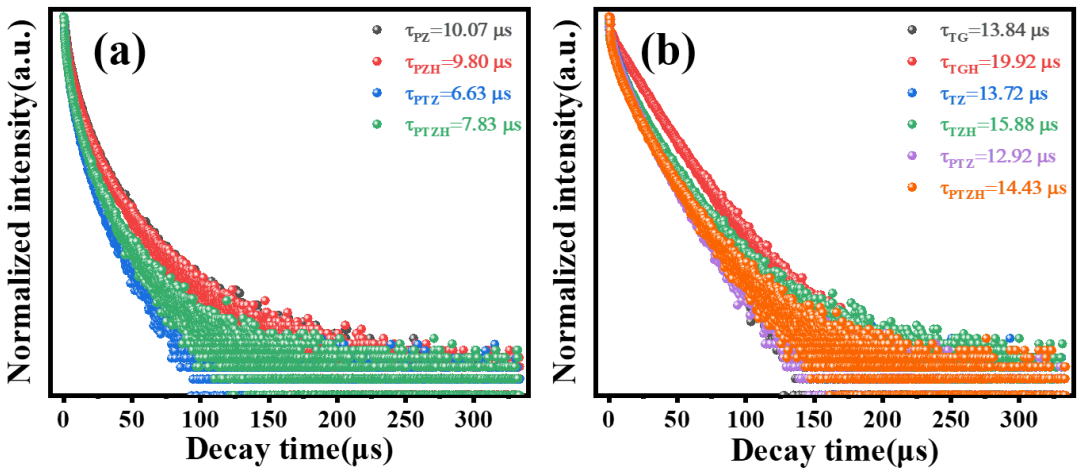

Figure 6. Decay curves of the different samples with the characteristic fluorescence at (a) 560 nm and (b) 458 nm.

The excitation spectra from 225 to 425 nm of the luminescent samples doped with Tm^{3+} ions are shown in Figure S6b. When 458 nm was used as the monitoring wavelength, the Tm^{3+} doped samples exhibited a strong narrow-band excitation peak near 358 nm, which could be attributed to the $^3H_6 \rightarrow {}^1D_2$ transition of Tm^{3+} [61]. The

three weak peaks at approximately 290, 275, and 262 nm in the excitation spectra of the TG, TGH, TZ, and TZH samples can be associated to the energy level transitions of Tm^{3+}:$^3H_6 \rightarrow {}^3P_0$, $^3H_6 \rightarrow {}^3P_1$, and $^3H_6 \rightarrow {}^3P_2$[61-62], respectively. The electrons excited to higher energy levels by UV radiation could return to $^1G_4$ or $^1D_2$ through non-RTs or RTs and to $^3H_6$ or $^3F_4$ through RTs, thus resulting in the emission at 478 and 458 nm, respectively. In addition, the PTZ and PTZH samples exhibited a broad excitation band in the range of 250–350 nm, and the TZ and TZH samples exhibited a similar excitation spectra, except that the intensity was weaker, which could be attributed to the excitation of the PbS QDs by UV light in this range. When the monitoring wavelength was 560 nm, the peak intensities of the excitation spectra of the PTZ and PTZH samples were reduced by varying degrees, which was consistent with the trend observed for the PZ and PZH samples. The decay curves and average decay lifetimes of the typical emissions from the Tm^{3+} ions and PbS QDs in different samples are shown in Figures 6a and 6b. The lifetime data were fitted with the third-order exponential decay model according to the following equation[63-64].

$$I = A_1 * \exp(-x/\tau_1) + A_2 * \exp(-x/\tau_2) + A_3 * \exp(-x/\tau_3) \quad (1)$$

where I is the relative fluorescence intensity; τ_i is the lifetime; and A_i is the coefficient of τ_i. The average lifetime was calculated using the following equation[63-64].

$$\tau_{average} = (A_1 * {\tau_1}^2 + A_2 * {\tau_2}^2 + A_3 * {\tau_3}^2)/(A_1 * \tau_1 + A_2 * \tau_2 + A_3 * \tau_3) \quad (2)$$

The key to obtaining high CRI white-light emission from this system is choosing

an appropriate excitation wavelength to simultaneously excite the characteristic emissions of the Tm^{3+} ions and PbS QDs and adjusting the relative intensities of the two emissions. The excitation-wavelength-dependent PL spectra of the PTZ and PTZH samples were recorded, as shown in Figure S8, to explore this phenomenon. When the excitation wavelength was 350 or 365 nm, both the PTZ and PTZH samples exhibited excellent white light characteristics. The CIE coordinates of PTZ at the two excitation wavelengths were (0.339, 0.3501) and (0.2999, 0.2744), CRI values reached 93.9 and 86.9, and color temperatures were 5236 and 8556 K, respectively. The CIE coordinates of the PTZH sample at the two excitation wavelengths were (0.3646, 0.3799) and (0.3329, 0.3131), CRI values were 90.1 and 93.7, and color temperatures were 4472 and 5464 K, respectively. The temperature-dependent PL spectra of the PTZ and PTZH samples at an excitation of 350 nm are shown in Figures 7a and 7d. The characteristic emissions of the Tm^{3+} ions and PbS QDs were gradually quenched with an increase in temperature from 293 to 473 K owing to thermally induced non-radiative de-excitation. However, the Tm^{3+} emission (~458 nm) exhibited a different temperature-dependent luminescence behavior compared to that of PbS (~560 nm). The emission intensity of the Tm^{3+} ions and PbS QDs exhibited a linear temperature dependence, whereas the Tm^{3+} ions emission was extremely insensitive to the changes in temperature. This phenomenon is reflected in the values of CIE coordinates, which indicated that as the temperature increased from 293 to 473 K, the color temperatures of PTZ and PTZH gradually increased from 5420 to 10966 K and from 4506 to 7618 K along the Planckian blackbody locus,

respectively. Additionally, the CIE coordinates of PTZ and PTZH gradually shifted from (0.3344, 0.3454) to (0.2796, 0.2763) and from (0.3634, 0.3791) to (0.2997, 0.3066), respectively, along the Planckian blackbody locus, as shown in Figures 7b and 7e, which can be used to effectively overcome the problem of chromatic aberration changes caused by changes in the working temperature. The CRI values of the PTZ sample did not follow a regular trend with the increase in temperature but were always greater than 91. In contrast, the CRI values of the PTZH sample gradually increased with increase in temperature and reached a maximum of 97, which suggests the potential for the fabrication of high-quality achromatic tunable white LED from this sample.

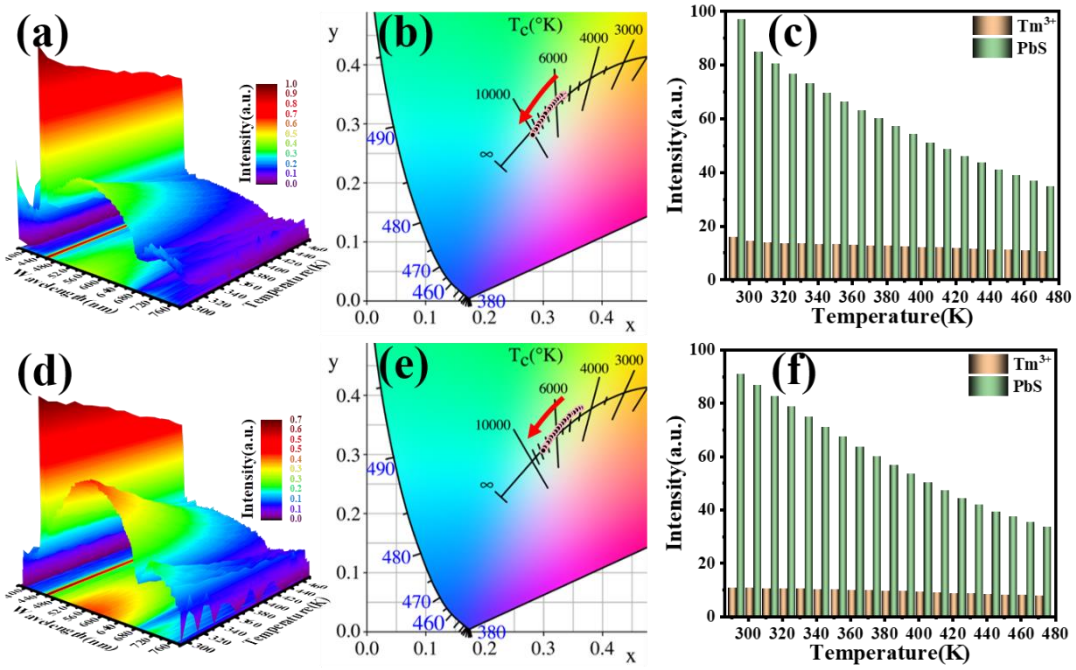

Figure 7. Temperature-dependent (293–473 K) PL spectra excited at 350 nm for the (a) PTZ and (d) PTZH samples. CIE coordinate diagrams of the (b) PTZ and (e) PTZH samples as a function of temperature. Integrated intensity histogram of the characteristic emissions of the (c) PTZ and (f) PTZH samples as a function of

temperature.

The application of PTZ and PTZH in the field of optical temperature sensing is discussed based on their different responses to temperature change. Figures 7c and 7f show the integrated intensity histogram of the characteristic emissions of the Tm^{3+} ions and PbS for the PTZ and PTZH samples in the temperature range of 293−473 K, respectively. The experimental curves of the fluorescence integrated intensity ratio (FIR) are shown in Figures 8a and 8c. The red solid lines are the fitting curves, which follow the following an empirical function[63-64].

$$FIR = I_{PbS}/I_{Tm^{3+}} \approx B + Aexp(C/kT) \quad (3)$$

where k is the Boltzmann constant; and A, B, and C are constants. As shown in Figures 8a and 8c, each fitting curve matches the experimental values well. The absolute and relative temperature sensitivities (S_a and S_r) were calculated as follows[63-64].

$$S_a = |\partial FIR/\partial T| = Aexp(C/kT) * (C/kT^2) \quad (4)$$

$$S_r = 100\% * \left|\frac{1}{FIR} * \frac{\partial FIR}{\partial T}\right| = 100\% * \frac{Aexp(-C/kT)}{B+Aexp(-C/kT)} * \frac{\Delta E}{kT^2} \quad (5)$$

The calculated S_a and S_r values of the PTZ and PTZH samples are shown in Figures 8b and 8d, respectively. For the PTZ sample, the maximum S_a and S_r values at 293 K were approximately 0.02688 K^{-1} and 0.42489 % K^{-1}, respectively. In contrast, the maximum S_a and S_r values of the heat-treated PTZH sample at 293 K, approximately

0.0391 K^{-1} and 0.45596 % K^{-1}, respectively, were slightly higher compared with the PTZ sample. This is only a preliminary result, and there is still much room for improvement. However, the results suggest the possibility of application of the RE-doped PbS QD glasses in optical temperature sensing, and currently, literature on the use of sulfide QD glasses for optical thermometers is limited.

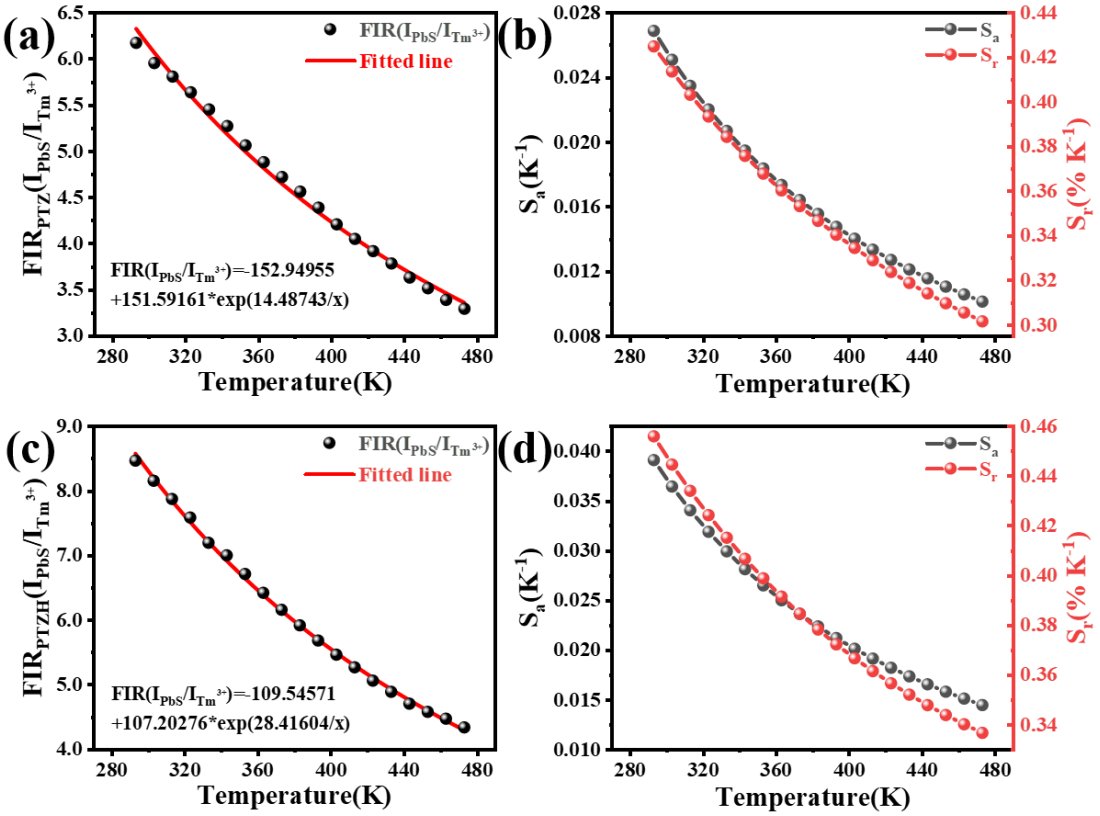

Figure 8. Experimentally obtained and fitted plots of FIR versus temperature of (a) PTZ and (c) PTZH. Calculated plots of S_a and S_r versus temperature of the (b) PTZ and (d) PTZH samples, respectively.

Conclusions

An optical color converter multicomponent inorganic glass embedded with PbS QDs was successfully fabricated via a facile melt-quenching method. The PbS QD-embedded glasses produced broad-band visible PL upon excitation with a UV source,

and reasonable color conversion capacity and variable CIE coordinates were obtained when the wavelength of the pump light was changed. Color-tunable white-light emission with high CRI values was obtained at 350 and 365 nm excitations by doping blue light emitting Tm^{3+} ions into the system. Thermal quenching analysis at an excitation of 350 nm revealed that as the temperature increased from 293 to 473 K, the CIE coordinates of PTZ and PTZH gradually shifted from (0.3344, 0.3454) to (0.2796, 0.2763) and (0.3634, 0.3791) to (0.2997, 0.3066), respectively, along the Planckian blackbody locus. The maximum S_a and S_r values of the PTZ sample were 0.02688 K^{-1} and 0.42489 % K^{-1} at 293 K, respectively. The maximum S_a and S_r values of the PTZH sample after HT increased to 0.0391 K^{-1} and 0.45596 % K^{-1} at 293 K, respectively. The present study reveals the potential application of inorganic glasses embedded with PbS QDs in multifunctional optoelectronic devices, such as high-CRI white LEDs, optical color converters, anti-counterfeiting, and optical thermometry.

Conflicts of interest

There are no conflicts to declare.

Acknowledgment

This work was supported by the National Natural Science Foundation of China (NSFC) (61975193 and U1909211).

References

1. García de Arquer, F. P.; Talapin, D. V.; Klimov, V. I.; Arakawa, Y.; Bayer, M.; Sargent, E. H., Semiconductor Quantum Dots: Technological Progress and Future Challenges. *Science* **2021**, *373, eaaz8541*.

2. Ferreira, R. A. S.; Correia, S. F. H.; Monguzzi, A.; Liu, X.; Meinardi, F., Spectral Converters for Photovoltaics – What's Ahead. *Mater Today* **2020**, *33*, 105-121.
3. Chen, J.; Zhao, H.; Li, Z.; Zhao, X.; Gong, X., Highly Efficient Tandem Luminescent Solar Concentrators based on Eco-friendly Copper Iodide Based Hybrid Nanoparticles and Carbon Dots. *Energ Environ Sci* **2022**, *15*, 799-805.
4. Zhao, H.; Liu, G.; You, S.; Camargo, F. V. A.; Zavelani-Rossi, M.; Wang, X.; Sun, C.; Liu, B.; Zhang, Y.; Han, G.; Vomiero, A.; Gong, X.; Gram-Scale Synthesis of Carbon Quantum Dots with a Large Stokes Shift for the Fabrication of Eco-Friendly and High-Efficiency Luminescent Solar Concentrators. *Energ Environ Sci* **2021**, *14*, 396-406.
5. Becker-Koch, D.; Albaladejo-Siguan, M.; Lami, V.; Paulus, F.; Xiang, H.; Chen, Z.; Vaynzof, Y., Ligand Dependent Oxidation Dictates the Performance Evolution of High Efficiency PbS Quantum Dot Solar Cells. *Sustain Energ Fuels* **2020**, *4*, 108-115.
6. Phuc, D. H.; Tung, H. T., Quantum Dot Sensitized Solar Cell Based on the Different Photoelectrodes for the Enhanced Performance. *Sol Energ Mat Sol C* **2019**, *196*, 78-83.
7. Crisp, R. W.; Pach, G. F.; Kurley, J. M.; France, R. M.; Reese, M. O.; Nanayakkara, S. U.; MacLeod, B. A.; Talapin, D. V.; Beard, M. C.; Luther, J. M., Tandem Solar Cells from Solution-Processed CdTe and PbS Quantum Dots Using a ZnTe-ZnO Tunnel Junction. *Nano Lett* **2017**, *17*, 1020-1027.
8. Yang, B.; Mei, S.; He, H.; Zhu, Y.; Hu, R.; Zou, J.; Xing, G.; Guo, R., Lead Oxide

Enables Lead Volatilization Pollution Inhibition and Phase Purity Modulation in Perovskite Quantum Dots Embedded Borosilicate Glass. *J Eur Ceram Soc* **2022**, *42*, 258-265.

9. Yu, X.; Zhang, H.; Yu, J., Luminescence Anti-Counterfeiting: From Elementary to Advanced. *Aggregate* **2021**, *2*, 20-34.
10. Li, H.; Zhang, W.; Bian, Y.; Ahn, T. K.; Shen, H.; Ji, B., ZnF_2-Assisted Synthesis of Highly Luminescent InP/ZnSe/ZnS Quantum Dots for Efficient and Stable Electroluminescence. *Nano Lett* **2022**, *22*, 4067-4073.
11. Li, M.; Wei, X.; Mei, S.; Cui, Z.; Fan, Y.; Yang, B.; Wen, Z.; Xiong, Z.; Wang, L.; Xie, F.; Zhang, W.; Guo, R., Highly Luminescent Copper Gallium Selenium based Multicomponent Quantum Dots: Formation Process and Tunable White-Light Emission. *Appl Surf Sci* **2021**, *538*, 147907.
12. Zhang, H.; Su, Q.; Chen, S., Quantum-Dot and Organic Hybrid Tandem Light-Emitting Diodes with Multi-Functionality of Full-Color-Tunability and White-Light-Emission. *Nat Commun* **2020**, *11*, 1-8.
13. Montanarella, F.; Kovalenko, M. V., Three Millennia of Nanocrystals. *ACS Nano* **2022**, *16*, 5085-5102.
14. Marin, R.; Jaque, D., Doping Lanthanide Ions in Colloidal Semiconductor Nanocrystals for Brighter Photoluminescence. *Chem Rev* **2021**, *121*, 1425-1462.
15. Pan, X.; Dong, Y.; Jia, M.; Wen, J.; Su, C.; Shang, Y.; Zhang, X.; Pang, F.; Wang, T., Temperature-Induced PbS Quantum Dots with Tunable Broadband Wavelength Grown by Atomic Layer Deposition. *Appl Surf Sci* **2021**, *546*, 149086.

16. Li, J.; Zhao, H.; Zhao, X.; Gong, X., Red and Yellow Emissive Carbon Dots Integrated Tandem Luminescent Solar Concentrators with Significantly Improved Efficiency. *Nanoscale* **2021**, *13*, 9561-9569.

17. Pradhan, N., Mn-Doped Semiconductor Nanocrystals: 25 Years and Beyond. *J Phys Chem Lett* **2019**, *10*, 2574-2577.

18. Dutta, A.; Pradhan, N., Phase-Stable Red-Emitting $CsPbI_3$ Nanocrystals: Successes and Challenges. *ACS Energy Lett* **2019**, *4*, 709-719.

19. Efros, A. L.; Brus, L. E., Nanocrystal Quantum Dots: From Discovery to Modern Development. *ACS Nano* **2021**, *15*, 6192-6210.

20. Xue, J.; Wang, X.; Jeong, J. H.; Yan, X., Fabrication, Photoluminescence and Applications of Quantum Dots Embedded Glass Ceramics. *Chem Eng J* **2020**, *383*, 123082.

21. Xia, M.; Luo, J.; Chen, C.; Liu, H.; Tang, J., Semiconductor Quantum Dots-Embedded Inorganic Glasses: Fabrication, Luminescent Properties, and Potential Applications. *Adv Opt Mater* **2019**, *7*, 1900851.

22. Wei, Y.; Ebendorff-Heidepriem, H.; Zhao, J., Recent Advances in Hybrid Optical Materials: Integrating Nanoparticles within a Glass Matrix. *Adv Opt Mater* **2019**, *7*, 1900702.

23. Esteve-Turrillas, F. A.; Abad-Fuentes, A., Applications of Quantum Dots as Probes in Immunosensing of Small-Sized Analytes. *Biosens Bioelectron* **2013**, *41*, 12-29.

24. Li, W.; Li, N.; Liu, C.; Greaves, G. N.; Ong, W. J.; Zhao, X., Understanding the Atomic and Electronic Structures Origin of Defect Luminescence of CdSe

Quantum Dots in Glass Matrix. *J Am Ceram Soc* **2019**, *102*, 5375-5385.

25. Vetchinnikov, M. P.; Lipatiev, A. S.; Shakhgildyan, G. Y.; Golubev, N. V.; Ignat'eva, E. S.; Fedotov, S. S.; Lipateva, T. O.; Lotarev, S. V.; Vilkovisky, G. A.; Sigaev, V. N., Direct Femtosecond Laser-Induced Formation of CdS Quantum Dots inside Silicate Glass. *Opt Lett* **2018**, *43*, 2519-2522.
26. Peng, Z.; Huang, X.; Ma, Z.; Dong, G.; Qiu, J., Surface Modification and Fabrication of White-Light-Emitting Tm^{3+}/CdS Quantum Dots Co-Doped Glass Fibers. *J Am Ceram Soc* **2019**, *102*, 5818-5827.
27. Li, W.; Zhao, X.; Liu, C.; Coudert, F. X., Ab Initio Molecular Dynamics of CdSe Quantum-Dot-Doped Glasses. *J Am Chem Soc* **2020**, *142*, 3905-3912.
28. Zhang, J.; Liu, C.; Heo, J., Mid-Infrared Luminescence from Sn-Modified PbSe Quantum Dots in Silicate Glasses. *J Non-Cryst Solids* **2016**, *431*, 93-96.
29. Litvin, A. P.; Babaev, A. A.; Dubavik, A.; Cherevkov, S. A.; Parfenov, P. S.; Ushakova, E. V.; Baranov, M. A.; Andreeva, O. V.; Purcell-Milton, F.; Gun'ko, Y.; Fedorov, A. V.; Baranov, A. V., Strong Enhancement of PbS Quantum Dot NIR Emission Using Plasmonic Semiconductor Nanocrystals in Nanoporous Silicate Matrix. *Adv Opt Mater* **2018**, *6*, 1701055.
30. Shao, X.; Wang, J.; Han, J.; Liu, C.; Ruan, J.; Zhao, X., Growth Kinetics and Optical Properties of PbSe Quantum Dots in Dual-Phase Lithium-Aluminum-Silicate Glass Ceramic. *J Eur Ceram Soc* **2020**, *40*, 4122-4128.
31. Huang, X.; Guo, Q.; Yang, D.; Xiao, X.; Liu, X.; Xia, Z.; Fan, F.; Qiu, J.; Dong, G., Reversible 3d Laser Printing of Perovskite Quantum Dots inside a Transparent

Medium. *Nat Photonics* **2020**, *14*, 82-88.

32. Ma, W.; Jiang, T.; Yang, Z.; Zhang, H.; Su, Y.; Chen, Z.; Chen, X.; Ma, Y.; Zhu, W.; Yu, X.; Zhu, H.; Qiu, J.; Liu, X.; Xu X.; Yang, Y. M., Highly Resolved and Robust Dynamic X-Ray Imaging Using Perovskite Glass-Ceramic Scintillator with Reduced Light Scattering. *Adv Sci* **2021**, *8*, e2003728.
33. Sun, K.; Tan, D.; Song, J.; Xiang, W.; Xu, B.; Qiu, J., Highly Emissive Deep-Red Perovskite Quantum Dots in Glass: Photoinduced Thermal Engineering and Applications. *Adv Opt Mater* **2021**, *9*, 2100094.
34. Liu, S.; Shao, G.; Ding, L.; Liu, J.; Xiang, W.; Liang, X., Sn-Doped $CsPbBr_3$ QDs Glasses with Excellent Stability and Optical Properties for WLED. *Chem Eng J* **2019**, *361*, 937-944.
35. Zhang, Y.; Liu, J.; Zhang, H.; He, Q.; Liang, X.; Xiang, W., Ultra-Stable Tb^{3+}: $CsPbI_3$ Nanocrystal Glasses for Wide-Range High-Sensitivity Optical Temperature Sensing. *J Eur Ceram Soc* **2020**, *40*, 6023-6030.
36. Chen, Z.; Zhao, J.; Zeng, R.; Liu, X.; Zou, B.; Xiang, W., High Efficiency Fluorescent Perovskite Quantum Dots Encapsulated in Superhydrophobic Silica Aerogel for Wide Color Gamut Backlight Displays. *Chem Eng J* **2022**, *433*, 133195.
37. Wang, Q.; Tong, Y.; Ye, H.; Liang, X.; Yang, K.; Xiang, W., Dual-Protective $CsPbX_3$ Perovskite Nanocomposites with Improved Stability for Upconverted Lasing and Backlight Displays. *ACS Sustain Chem Eng* **2021**, *9*, 11548-11555.
38. Xiong, Y.; Liu, C.; Wang, J.; Han, J.; Zhao, X., Near-Infrared Anti-Stokes

Photoluminescence of PbS QDs Embedded in Glasses. *Opt Express* **2017**, *25*, 6874-6882.

39. Huang, X.; Peng, Z.; Guo, Q.; Song, X.; Qiu, J.; Dong, G., Energy Transfer Process and Temperature-Dependent Photoluminescence of PbS Quantum Dot-Doped Glasses. *J Am Ceram Soc* **2018**, *102*, 3391-3401.
40. Xu, Z.; Yan, J.; Xu, C.; Cheng, C.; Jiang, C.; Liu, X.; Qiu, J., Tunable near-Infrared Emission and Fluorescent Lifetime of PbSe Quantum Dot-Doped Borosilicate Glass. *J Alloy Compd* **2017**, *711*, 58-63.
41. Guerreiro, P. T.; Ten, S.; Borrelli, N. F.; Butty, J.; Jabbour, G. E.; Peyghambarian, N., PbS Quantum-Dot Doped Glasses as Saturable Absorbers for Mode Locking of a Cr:Forsterite Laser. *Appl Phys Lett* **1997**, *71*, 1595-1597.
42. Moreels, I.; Lambert, K.; Smeets, D.; De Muynck, D.; Nollet, T.; Martins, J. C.; Vanhaecke, F.; Vantomme, A.; Delerue, C.; Allan, G., Size-Dependent Optical Properties of Colloidal PbS Quantum Dots. *ACS nano* **2009**, *3*, 3023-3030.
43. Hines, M. A.; Scholes, G. D., Colloidal PbS Nanocrystals with Size-Tunable near-Infrared Emission: Observation of Post-Synthesis Self-Narrowing of the Particle Size Distribution. *Adv Mater* **2003**, *15*, 1844-1849.
44. Zhang, R.; Lin, H.; Yu, Y.; Chen, D.; Xu, J.; Wang, Y., A New-Generation Color Converter for High-Power White LED: Transparent Ce^{3+}: YAG Phosphor-in-Glass. *Laser Photonics Rev* **2014**, *8*, 158-164.
45. Hossain, M. K.; Hossain, S.; Ahmed, M. H.; Khan, M. I.; Haque, N.; Raihan, G. A., A Review on Optical Applications, Prospects, and Challenges of Rare-Earth

Oxides. *ACS Appl Electron Ma* **2021**, *3*, 3715-3746.

46. Zheng, B.; Fan, J.; Chen, B.; Qin, X.; Wang, J.; Wang, F.; Deng, R.; Liu, X., Rare-Earth Doping in Nanostructured Inorganic Materials. *Chem Rev* **2022**.
47. Brites, C. D. S.; Balabhadra, S.; Carlos, L. D., Lanthanide-Based Thermometers: At the Cutting-Edge of Luminescence Thermometry. *Adv Opt Mater* **2019**, *7*, 1801239.
48. Wang, Z.; Huang, F.; Li, D.; Lei, R.; Zhang, J.; Xu, S., An Environmental Amorphous Solid by Local Crystallization for Multifunctional Optical Applications. *J Clean Prod* **2020**, *270*, 122441.
49. Zhou, S.; Li, C.; Yang, G.; Bi, G.; Xu, B.; Hong, Z.; Miura, K.; Hirao, K.; Qiu, J., Self-Limited Nanocrystallization-Mediated Activation of Semiconductor Nanocrystal in an Amorphous Solid. *Adv Funct Mater* **2013**, *23*, 5436-5443.
50. Kang, S.; Ouyang, T.; Yang, D.; Pan, Q.; Qiu, J.; Dong, G., Enhanced 2 μm Mid-Infrared Laser Output from Tm^{3+}-Activated Glass Ceramic Microcavities. *Laser Photonics Rev* **2020**, *14*, 1900396.
51. Lin, S.; Lin, H.; Ma, C.; Cheng, Y.; Ye, S.; Lin, F.; Li, R.; Xu, J.; Wang, Y., High-Security-Level Multi-Dimensional Optical Storage Medium: Nanostructured Glass Embedded with $LiGa_5O_8$: Mn^{2+} with Photostimulated Luminescence. *Light Sci Appl* **2020**, *9*, 1-10.
52. Zhou, S.; Jiang, N.; Miura, K.; Tanabe, S.; Shimizu, M.; Sakakura, M.; Shimotsuma, Y.; Nishi, M.; Qiu, J.; Hirao, K., Simultaneous Tailoring of Phase Evolution and Dopant Distribution in the Glassy Phase for Controllable

Luminescence. *J Am Chem Soc* **2010**, *132*, 17945-17952.

53. Yin, Q.; Zhang, W.; Zhou, Y.; Wang, R.; Zhao, Z.; Liu, C., High Efficiency Luminescence from PbS Quantum Dots Embedded Glasses for near-Infrared Light Emitting Diodes. *J Lumin* **2022**, 119065.
54. Li, K.; Ye, Y.; Zhang, W.; Hu, Y.; Yang, Y.; Zhou, Y.; Liu, C., Modulation of the Optical Properties of ZnS QD-Embedded Glass through Aluminum and Manganese Doping. *J Mater Chem C* **2021**, *9*, 11261-11271.
55. Chang, L.; He, X.; Chen, L.; Zhang, Y., Mercaptophenylboronic Acid-Capped Mn-Doped ZnS Quantum Dots for Highly Selective and Sensitive Fluorescence Detection of Glycoproteins. *Sensor Actuat B Chem* **2017**, *243*, 72-77.
56. Karan, N. S.; Sarkar, S.; Sarma, D. D.; Kundu, P.; Ravishankar, N.; Pradhan, N., Thermally Controlled Cyclic Insertion/Ejection of Dopant Ions and Reversible Zinc Blende/Wurtzite Phase Changes in ZnS Nanostructures. *J Am Chem Soc* **2011**, *133*, 1666-9.
57. Fan, S.; Wu, G.; Zhang, Y.; Chai, G.; Ma, Z.; Qiu, J.; Dong, G.; Heo, J., Novel Visible Emission and Mechanism Investigation from PbS Nanoclusters-Doped Borosilicate Glasses. *J Am Ceram Soc* **2014**, *97*, 173-178.
58. Yu, J., et al., Broadband Extrinsic Self-Trapped Exciton Emission in Sn-Doped 2d Lead-Halide Perovskites. *Adv Mater* **2019**, *31*, e1806385.
59. Han, Y.; He, S.; Luo, X.; Li, Y.; Chen, Z.; Kang, W.; Wang, X.; Wu, K., Triplet Sensitization by "Self-Trapped" Excitons of Nontoxic $CuInS_2$ Nanocrystals for Efficient Photon Upconversion. *J Am Chem Soc* **2019**, *141*, 13033-13037.

60. Klimesz, B.; Lisiecki, R.; Ryba-Romanowski, W., Thermosensitive Tm^{3+}/Yb^{3+} Co-Doped Oxyfluorotellurite Glasses – Spectroscopic and Temperature Sensor Properties. *J Alloy Compd* **2020**, *823*, 153753.

61. Erol, E.; Kıbrıslı, O.; Ersundu, M. Ç.; Ersundu, A. E., Color Tunable Emission from Eu^{3+} and Tm^{3+} Co-Doped $CsPbBr_3$ Quantum Dot Glass Nanocomposites. *Phys Chem Chem Phys* **2022**, *24*, 1486-1495.

62. Li, X.; Yu, Y.; Guan, X.; Luo, P.; Chen, F.; Yu, M.; Jiang, L., Dual-Emitting Tm^{3+}/Mn^{2+} Co-Doped Glass Ceramic for Wide-Range Optical Thermometer. *J Alloy Compd* **2020**, *836*, 155507.

63. Wu, M.; Deng, D.; Ruan, F.; Chen, B.; Xu, S., A Spatial/Temporal Dual-Mode Optical Thermometry Based on Double-Sites Dependent Luminescence of $Li_4SrCa(SiO_4)_2$: Eu^{2+} Phosphors with Highly Sensitive Luminescent Thermometer. *Chem Eng J* **2020**, *396*, 125178.

64. Xue, J.; Noh, H. M.; Choi, B. C.; Park, S. H.; Kim, J. H.; Jeong, J. H.; Du, P., Dual-Functional of Non-Contact Thermometry and Field Emission Displays Via Efficient $Bi^{3+} \rightarrow Eu^{3+}$ Energy Transfer in Emitting-Color Tunable $GdNbO_4$ Phosphors. *Chem Eng J* **2019**, 122861.

Graphical abstract

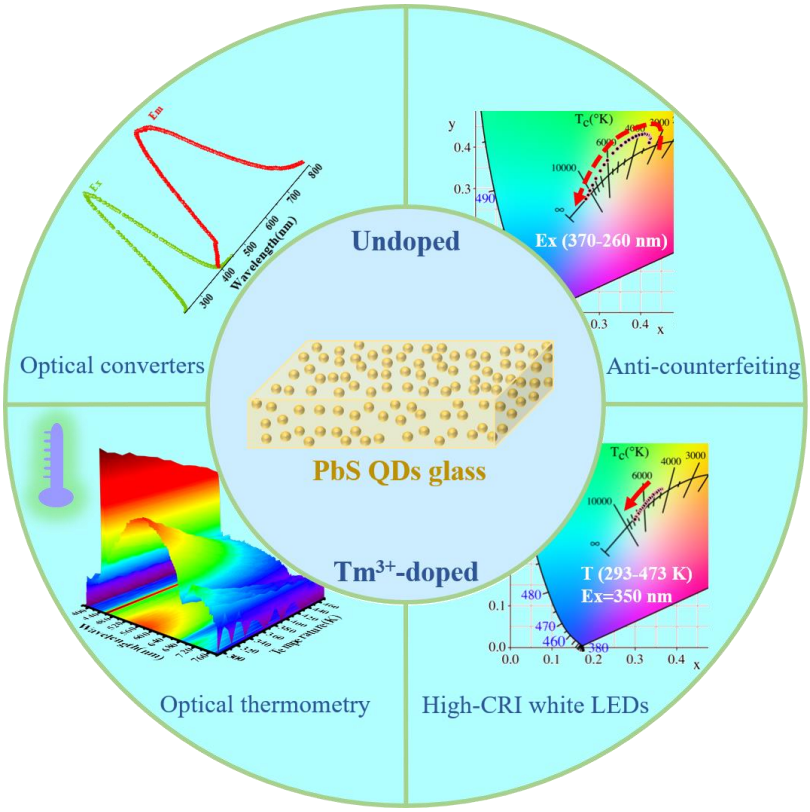

CRediT authorship contribution statement

Zheng Wang: Conceptualization, Data curation, Writing-Original draft preparation;

Jiabo Li：Investigation, Visualization;

Feifei Huang: Methodology, Writing-Reviewing & Editing;

Youjie Hua: Resources, Formal analysis;

Ying Tian: Validation;

Xianghua Zhang: Supervision;

Shiqing Xu: Funding acquisition, Project administration.

Declaration of interests

☒ The authors declare that they have no known competing financial interests or personal relationships that could have appeared to influence the work reported in this paper.

☐The authors declare the following financial interests/personal relationships which may be considered as potential competing interests:

Highlights：

1: PbS QDs were successfully prepared in an inorganic glass with broad-band emission.

2: Variable emission of PbS QDs glass at different UV excitation were obtained.

3: High CRI white light was obtained by combining the emission of PbS QDs with Tm ions.

4: A novel optical thermometer based on the inorganic PbS QDs glasses was revealed.